INVITED PAPER

Superlattice Infrared Photodetector Research at the Jet Propulsion Laboratory

S. D. Gunapala, D. Z. Ting, S. B. Rafol, A. Soibel, A. Khoshakhlagh, C. J. Hill, L. Höglund, S. A. Keo, J. K. Liu, J. M. Mumolo, E. M. Luong, and A. Fisher

Center for Infrared Photodetectors, Jet Propulsion Laboratory, California Institute of Technology, 4800 Oak Grove Drive, Pasadena, CA 91109

ABSTRACT

III-V semiconductors offer a highly effective platform for the development of sophisticated heterostructure-based MWIR and LWIR detectors, as exemplified by the high-performance double heterstructure (DH) nBn, XBn, and type-II superlattice infrared detectors. A key enabling design element is the unipolar barrier, which is used to implement the complementary barrier infra-red detector (CBIRD) design for increasing the collection efficiency of photo-generated carriers, and reducing dark current generation without impeding photocurrent flow. Heterostructure superlattice detectors that make effective use of unipolar barriers have demonstrated strong reduction of generation-recombination (G-R) dark current due to Shockley-Read-Hall (SRH) processes. In the last several years we solely focused on the development of antimonide based IR detectors. Recently, we demonstrated RoA values over 14,000 Ohm cm^2 for a 9.9 μm cutoff device by incorporating electron-blocking and hole-blocking unipolar barriers. This device has shown 300K BLIP operation with f/2 optics at 87 K with blackbody D^* of 1.1×10^{11} cm $Hz^{1/2}$/W.

Keywords: Infrared, focal planes, superlattice, long-wave infrared

1. INTRODUCTION

Jet Propulsion Laboratory has been working on III-V quantum structures for infrared (IR) detection since early nineties. III-V material systems are very attractive for the fabrication of large area IR detector arrays due to its mature growth and processing techniques and availability of low cost epi-ready III-V substrates. There are many applications that require long wavelength, large, uniform, reproducible, low cost, stable, and radiation-hard IR focal plane arrays (FPAs). For example, the absorption lines of many gas molecules, such as ozone, water, carbon monoxide, carbon dioxide, and nitrous oxide occur in the wavelength region from 3 to 15 μm. Thus, IR imaging systems that operate in the mid- and long-wavelength IR regions are required in many space borne applications such as monitoring the global atmospheric temperature profiles, relative humidity profiles, cloud characteristics, and the distribution of minor constituents in the atmosphere which are being planned for future NASA Earth and planetary remote sensing systems.

The demand for high performance infrared sensors will increase, especially for high frame rate and high-resolution third generation systems to detect and identify targets at long distances. Detection and identification at large distance depend on the lowest achievable dark current and highest quantum efficiency. There are few high performance IR technologies that are currently available for middle wave infrared (MWIR, 3-5μm), long wave infrared (LWIR, 8-12 μm) and very long wave infrared (VLWIR, > 12 μm) applications. However, the choice of which technology to employ depends on the application and cost. II-VI material based IR technology and III-V material Quantum Well Infrared Photoconductor (QWIP) are currently the available technologies which cover both the MWIR and LWIR spectral band, but each technology has its own limit [1]. II-VI sensors are high performance, but are limited by the technology. On the other hand QWIP has low quantum efficiency (QE), which precludes its application to slow frame rate (detector system-limited). An alternative technology is the Type-II Superlattice (SL) IR sensor which has performance that is currently at the level between II-VI and III-V QWIP. However, Type-II SL has the potential to achieve the same performance as the II-VI material [2]. Because of the availability of relatively low cost large substrate, matured growth technology, and many processing foundries, this technology has tremendous potential for very large format, highly uniform (FPAs) at a lower cost [3]. Type-II SL has the advantage similar to QWIP in pixel operability and uniformity, but at a higher QE. Band gap engineering also makes it possible to design, grow and

process type II SL detectors arrays that can interface with different read out integrated circuit (ROICs) and operate at higher temperatures. The rapid progress on this technology has demonstrated that type-II LWIR SL based FPA has potential for high performance [4,5]. The major advantage of the III-V technology is the simplicity to grow and process the material. However, it still has some technological issues related to dark current, QE and lifetime [6]. Current research and development efforts on Type-II SL are addressing these issues [7,8].

2. CBIRD DEVICE STRUCTURE

The complementary barrier infrared detector (CBIRD) structure needs n on p ROIC as an electrically interface since it provides electrons at the top contact. This CBIRD design consists of a 300-period (44 Å, 21 Å)-InAs/GaSb absorber superlattice (SL) sandwiched between an 80-period (46 Å, 12 Å)-InAs/AlSb hole-barrier (hB) SL on the left and 60-period (22 Å, 21 Å)-InAs/GaSb electro-barrier (eB) SL on the right. The hB SL and eB SL are, respectively, designed to have approximately zero conduction and valence band offset with respect to the absorber SL. The hB SL is doped at $n=1x10^{16}$ cm^{-3} while the absorber SL and eB SL are nominally doped at $p=1x10^{16}$ cm^{-3}, and $p=1x10^{16}$ cm^{-3} [9.10]. $InAs_{0.91}Sb_{0.09}$ adjacent to the eB acts as the V_{DET_COM} contact layer, and the hB SL serves as the top contact layer that is electrically connected to the ROIC. For CBIRD the V_{DET_COM} is at a lower potential relative to the top contact or ROIC. This injects electrons into the ROIC and the mode is n on p. The dry etching process was utilized to fabricate the 320 x 256 pixel arrays with 30 μm pixel pitch. FLIR/Indigo two-color direct injection 320x256 pixel format ISC0903 ROIC [11] was used to fabricate FPAs. The detector arrays and ROICs were hybridized using the SET FC-300 flip-chip bonder. After hybridization, the FPAs were backfilled with epoxy and cured overnight. The substrate was completely removed by mechanical lapping followed by the dry etch process all the way down to the etch stop layer.

3. TESTING AND CHARACTERIZATION OF CBIRD FPA

The FPA was cooled down to 78K and 65K for data acquisition at two temperatures. Figure 1 shows the plot of mean external QE as a function of wavelength, which is measured directly from the FPA at 78K, 128 mV bias, and 370 μsec integration time. The maximum QE of 54 % has been achieved for double pass geometry. This is slightly lower than the single element result. The FPA is back illuminated while the single element test device is front-illuminated. The substrate was completely removed and thinned enough to be transparent for IR radiation. The cut-off wavelength is about 8.8 μm, which is at 50% of the peak, and the Full-Width-Half-Maximum (FWHM) is from roughly from 4.4 μm to 8.8 μm. The mean responsivity is 46.2 nV/photon with operability of 97%. The operability is defined as those pixels with responsivity between 20% and 150% of the mean responsivity. The low responsivity can be partially attributed to low ROIC gain which is ~97nV/electron [11].

Figure 2 depicts the dark current density histogram at an operating bias of 128 mV. The integration time was set slightly higher to 490 μsec, which should not affect the dark current estimate. The mean dark current density of ~2.2 x 10^{-4} A/cm^2 is a factor of 4.4 higher than the mean measured dark current from many single element devices at the same temperature and bias. Estimates show that at 240K background temperature the dark current density is comparable to photocurrent density from 298K background. The mean dark current density of the large area single element detectors at ~77K was ~ 5 x 10^{-5} A/cm^2. The FPA detector array is not passivated and surface conduction may have contributed to the increase in dark current density.

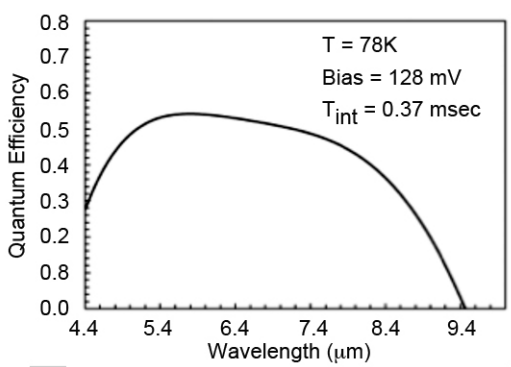

Fig. 1. Quantum efficiency spectrum of long-wavelength superlattice CBIRD device. Quantum efficiency was measured with double-pass geometry.

Excess dark current normally originates from generation-recombination, trap assisted tunneling, and surface leakage [5]. However, when the temperature was lowered to 65K, the mean dark current density decreased to 1.1 x 10^{-4} A/cm^2. This implies that there is a surface leakage in addition to the bulk current. However, the bulk dark current density still dominates considerably and decreases with temperature. The decreasing bulk dark current density as a function of decreasing temperature clearly indicates the absence of trap assisted tunneling assuming the surface leakage current is independent of temperature. The uncorrected spatial non-uniformity (sigma/mean) at 298K blackbody temperature is 5.5%. The temporal NEΔT matrix is numerically evaluated from the relations, NEΔT = $\sigma_{Temporal}\Delta T/[Mean(T_H) - Mean(T_L)]$ [6]. The matrices Mean(T_L) and Mean(T_H) are the means evaluated at blackbody temperatures of T_L = 293 K and T_H = 303K. The temporal noise is estimated at 298K using 32 frames, and ΔT ~10K. The experimentally measured NEΔT histograms distributions of the CBIRD FPA at 78K operating temperature, 128 mV bias, and 370 μsec integration time, with blackbody temperature of 298K and an f/2 cold stop, is shown in the Fig. 3. The mean NEΔT of 18.6 mK and 12 mK is achieved at FPA operating temperatures of 78K and 65K respectively. This means that noise has decreased with temperature.

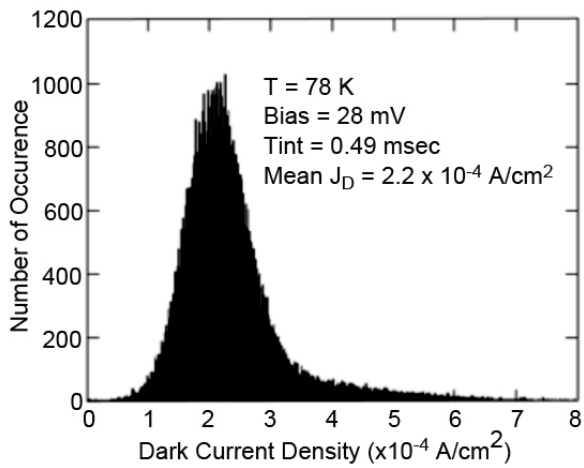

Fig. 2. Dark current of CBIRD FPA at a bias of 128 mV and 78K operating temperature.

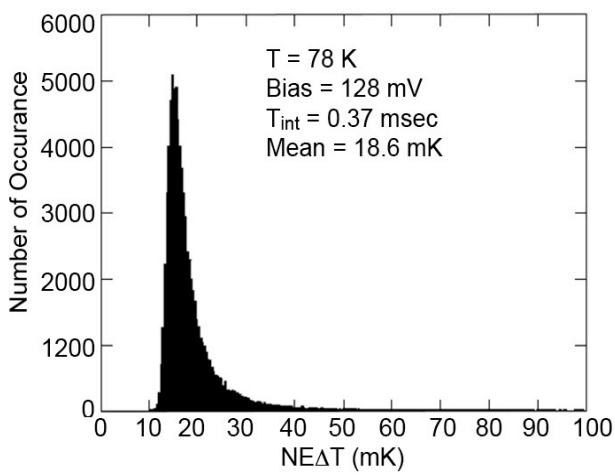

Fig. 3. Measured CBIRD NEΔT histogram operating at 78K, bias of 128 mV and integration time of 370 μsec. The mean NEΔT is 18.6 mK.

4. MRΔT AND MTF OF CBIRD FPA

In this section we describe the minimum resolvable temperature difference (MRΔT) and MTF measurements. Figure 4(a) and (b) depict MRΔT and MTF plots of an LWIR CBIRD FPA respectively. MRΔT is a subjective measurement of an FPA image using trained human observers. It requires a stable differential temperature between background and a four bar target that will produce a unity signal-to-noise ratio on the display monitor as a function of target spatial frequency [1]. This measures thermal sensitivity as a function of spatial resolution defined by the four bar target with aspect ratio of 7:1. The period of the four bar target is varied and the spatial frequency is estimated for each four bar target. At small spatial frequency, the horizontal MRΔT (HMRΔT) and vertical MRΔT (VMRΔT) are slightly lower than the NEΔT value, which is also shown on the MRΔT plot. At higher spatial frequency, it requires a larger temperature difference to generate a contrast between the four bar targets and background. Positive and negative contrast was measured and temperature difference was averaged to eliminate the offset. The four bar target becomes difficult to resolve at 15.89 cycles/mm (which is just below Nyquist frequency ~16.67cycles/mm) in both the vertical and horizontal direction even after moving the target slightly to compensate ***for the phasing effect and raising the temperature of the background*** [12,13]. It is observed that only three bars were apparent instead of four and two of the bars merge into one at a frequency close to Nyquist.

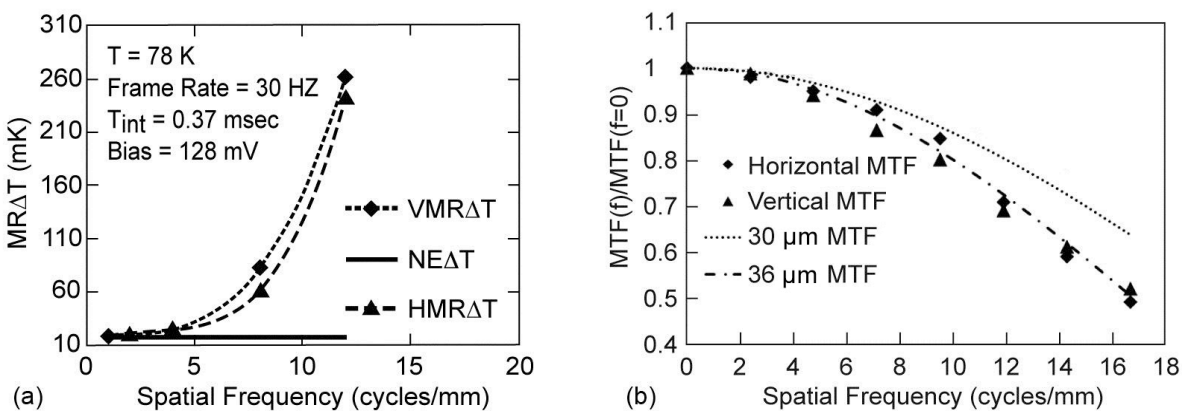

Fig. 4. (a) Minimum Resolvable Temperature Difference (MRΔT) and (b) Modulation Transfer Function (MTF) as a function of spatial frequency measured from 320 x 256 CBIRD FPA operating at 78K, at a bias at 128 mV and integration time of 370 μsec.

MTF technically provides a measure of image resolution or spatial frequency response of the infrared imaging system. It is a measure of how the contrast is transferred from object space to image space as a function of spatial frequency. MTF is inversely related to MRΔT [13]. The ESF is then constructed as previously described. The ESF is numerically differentiated to obtain the LSF. The zero frequency normalized absolute value of the Fourier transform of the LSF is the one dimensional MTF of the system. The lens MTF is removed by dividing the measured MTF with the lens MTF. The plot in Figure 4(b) is MTF(f)/MTF(F=0) of the FPA and electronics in horizontal and vertical orientation.

The higher MTF at low frequency produces better contrast (see Figure 14) and, therefore better images are observed at low spatial frequency. Higher MTF values at high frequency produce good quality images at higher frequency. The horizontal and vertical MTFs at Nyquist frequency based on pixel pitch, a, (= 1/2a, a = 30μm) ~16.67cycles/mm are about ~0.49 and ~0.52, respectively. The Nyquist frequency is well below the optical cut off frequency of ~56.8 cycles/mm based on the 8.8 μm detector cut off wavelength. The loss of MTF can be due to defocusing [4-5, 7] and this defocusing effect is eliminated by acquiring data at the best focus and then collecting data by moving the FPA by ± 50 μm along the optical axis from the best focus location. This is roughly the size of the Airy disk.

The FPA MTF can be separated into the product of two components. The geometric aperture MTF is related to the pixel size and the diffusion MTF related to electro-optical properties [12-20]. The diffusion MTF depends on the diffusion length and geometry. The carrier diffusion degrades high frequency MTF and manifests as crosstalk (or MTF loss). However, the CBIRD pixels are delineated down to the bottom contact and it is expected that no lateral carrier diffusion into the next neighbor can occur. The advantage of delineation is the reduction of cross talk. The disadvantage (in non-planar device structures) is that the fill factor is less than 100%. Shorter wavelengths on the other hand can be absorbed near the top surface and can diffuse to the next neighbor. In CBIRD FPA, the only channel left for the charge carriers to diffuse to an adjacent pixel is through the thin VDET_COM layer.

The geometric aperture MTF can be estimated using a sinc function. Since the pixel is square, the aperture MTF is the same in the horizontal and vertical orientation. For a pixel pitch of 30μm, the CBIRD FPA pixel size, a sinc function describing an aperture MTF is plotted in Fig. 4(b). Smaller pixel size actually improves high frequency MTF since at Nyquist (sampling using FPA pitch) its value is greater than 0.64. The difference between aperture MTF and the measured MTF is the upper limit on the diffusion MTF (crosstalk) since other MTF components such as electronic and other effects are not known completely as well as surface recombination. The ROIC crosstalk is small, ~ 0.1% by design. At Nyquist frequency, the difference between measured horizontal/vertical and the ideal MTF is ~0.14, but at low frequencies the difference is small. The MTF loss is basically an effective increase of the pixel size. The geometric aperture MTF function decreases with increasing pixel size and frequency. Thus detectors can be viewed as an overlapping Gaussian-like array. For example, the matching pixel size that matches closely with the MTF data (horizontal and vertical) in Fig. 4 is approximately 36 μm which is larger than the pitch. Imagery was performed at 78K FPA operating temperature and Fig. 5 shows outside natural scenery. The image quality of the natural scene attests to the very good MTF behavior at low and high frequencies. This FPA gave good images, with more than 97% of the pixels operable. Video images were taken at a frame rate of 30 Hz and integration time of 0.37 msec.

Fig. 5. Outside images taken with the long-wavelength infrared CBIRD superlattice focal plane array. The FPA is operated at 78K with NEΔT of 18.6 mK with f/2 optics at 300K background. This image show good quality reproduction of low and high spatial frequency.

5. IMPROVED CBIRD (i-CBIRD)

An improved-CBIRD (i-CBIRD) structure with the double broken-gap junction bottom contact design was grown on a 50-mm diameter Te-doped GaSb (100) substrate in a Veeco Applied-Epi Gen III molecular beam epitaxy chamber equipped with valved cracking sources for the group V Sb2 and As2 fluxes. The active region of the structure consists of a 300-period (44A°, 21A°) InAs/GaSb absorber SL sandwiched between an 80-period (46A°,12A°)-InAs/AlSb hB SL on top and a 60-period (22A°, 21A°)-InAs/GaSb eB SL on the bottom. The active region is separated from the p-GaSb bottom contact by a 0.2 μm $InAs_{0.91}Sb_{0.09}$ layer. The hB SL and absorber SL are nominally doped at $n=1x10^{16}$ cm^{-3} and $p=1x10^{16}$ cm^{-3}, respectively. The p-type eB SL is doped $2\mathbf{x}10^{16}$ cm^{-3} at the top, then graded up to $1x10^{18}$ cm^{-3}

on bottom. The n-InAsSb layer is doped $1x10^{18}$ cm^{-3} at the top and graded up to $1x10^{19}$ cm^{-3} on bottom. The doping in the p-GaSb bottom contact is ramped down from $1x10^{19}$ cm^{-3} near the InAsSb side to $5x10^{17}$ cm^{-3}. Square mesa photodiodes of area 200 µm x 200 µm were fabricated using a dry etch process for responsivity and dark current measurements. The devices were not passivated nor treated with anti-reflection coating.

Figure 5 shows the spectral QE derived from spectral responsivity measured at 77K under 0.1V bias, assuming unity gain. Also shown is the 77K photoluminescence (PL) spectrum. We caution that since the responsivity measurement is taken with a top illuminated sample resting on a reflecting metallic surface of the chip carrier, and that the GaSb substrate is partially transmitting (more so in the mid-wave than LWIR), our measured spectral response contains contributions from light re-entering the absorber region after reflecting off the bottom surface. The PL peak is at 9.6 µm (0.129 eV), while the 50% peak QE cutoff wavelength occurs at 9.83 µm (0.126 eV). The band gap inferred from the spectral QE inflection point is 0.121 eV (10.2 µm). The inset plots the peak QE as a function of applied bias at 77K and shows that the photoresponse is fully turned on at zero bias. This is in contrast to the original CBIRD reported in Ref. 9, which required close to 250 mV to turn on fully.

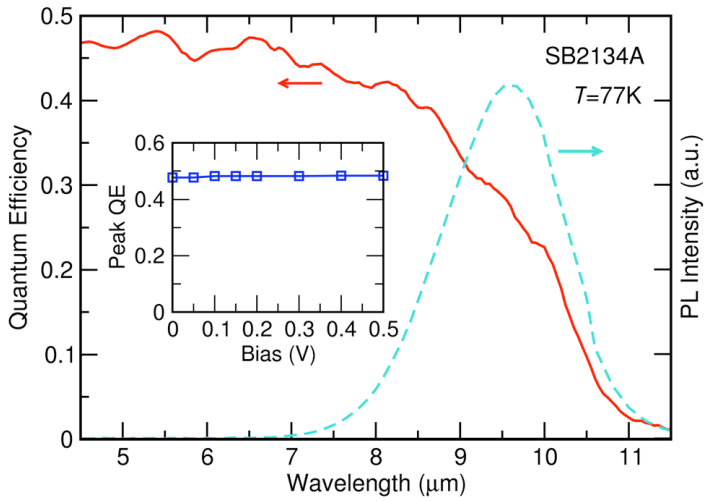

Fig. 6. PL spectrum and top illuminated spectral QE for a i-CBIRD device measured at 77K. The inset shows the peak QE as a function of applied bias. (After Ref. 21)

Figure 7 shows the measured dark current density as a function of applied bias for temperatures ranging from 19K to 165 K. Tunneling dark current, most likely due to trapassisted tunneling [21], appears to be dominant at 55K and below and is still apparent at 73K under higher reverse (positive) bias. The inset shows an Arrhenius plot of the temperature dependence of dark current density under 0.1V bias. A fit to the expression $CT^3 \exp(-\Delta E/k_B T)$ yields an activation energy of ΔE=0.112 eV, which is somewhat lower but close to the band gap, indicating near diffusion-limited dark current behavior. The estimated dark current density at 77K is $7.95x10^{-6}$ A/cm^2, which is only a factor of 2 or 4 (depending on whether we take the 77K cutoff to be at 9.83 µm or 10.2 µm) higher than predicted by the MCT Rule 07. To be fair, the i-CBIRD absorber would have to be made thicker to achieve the QE level typically associated with the MCT Rule 07 and would therefore have proportionally higher diffusion dark current. Nevertheless, the i-CBIRD dark current performance is still quite good. The experimental results indicate that the i-CBIRD design performs as well as the original CBIRD [9]. The only notable difference is the lowering of the turn-on bias, which requires further explanation as it is very unlikely to be due to the modified bottom contact design. The dark current performance of i-CBIRDs in general is also somewhat puzzling. Donetsky *et al.*[22] measured 77K SRH lifetimes in a p –type T2SL (E_g =0.12 eV) and an n -type MCT (E_g =0.11 eV) samples and obtained 31 ns and 1 µs, respectively. Thus, it is important to understand why do generation-recombination (G-R) processes not have a larger contribution to the CBIRD dark current. Even if G-R dark current is somehow suppressed, why is the diffusion-limited dark current of CBIRD so close to that of MCT when there is such a large difference in minority carrier lifetimes? This is clearly explained by Ting *et al*. in Ref. 22. The dark current density vs. voltage curves for i-CBIRD are shown in Fig. 7.

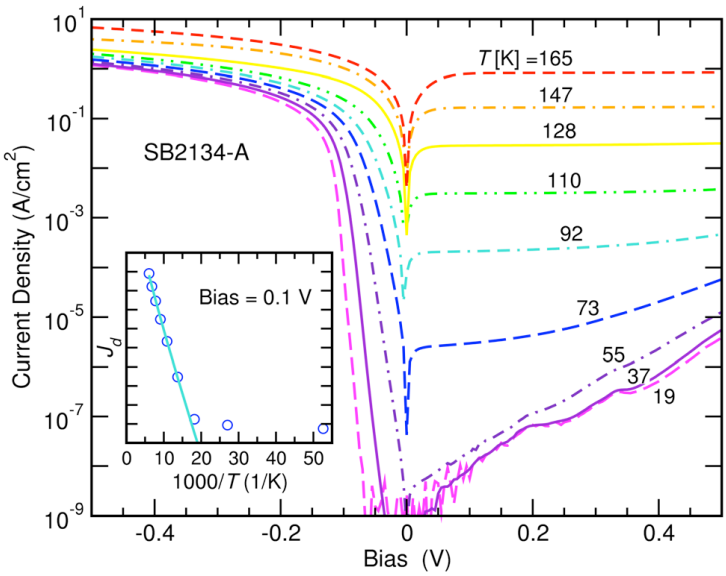

Fig. 7 Dark current density (J_d) as a function of applied bias, measured at various temperatures ranging from 19K to 165 K. The inset shows temperature dependence of Jd (over the same range as the main plot) at 0.1V bias. (After Ref. 21)

With the T2SL having substantially shorter minority carrier lifetime than MCT, the observed diffusion-limited dark current of CBIRD is surprisingly low. The diffusion dark current density from the p-side of a pn diode is given approximately by $J_{e:iff.} = qn_0 L / \tau_n$, where n_0 is the minority carrier density in the diffusion layer, L is the diffusion length (or absorber layer width), and τ_n, is the minority carrier (electron) lifetime. Assuming (quasi-) equilibrium conditions, the expression can also be written as $J_{e:iff.} = qn_i^2 L / N_a \tau_n$, where N_a is the acceptor dopant density. In the CBIRD absorber SL, we use N_a =1x10^{16} cm^{-3}, which is noticeably higher than the doping level found in LWIR MCT detectors (typically low 10^{15} cm^{-3}). Higher doping is permitted in SL because of tunneling suppression. The higher doping compensates in part for the shorter lifetime, resulting in relatively low diffusion dark current. (We note that the higher doping probably contributed to the shorter lifetime in the first place.) Another reason for the observed low dark current density is minority carrier exclusion (by the electron barrier) and extraction (at the hole barrier–absorber junction), rendering minority carrier density lower than equilibrium values [22]. In the absorber region, the majority carrier (hole) concentration is given by the dopant level and is unperturbed by applied bias; this keeps the G-R dark current in check. The minority carrier (electron) density falls to more than two orders of magnitude below the equilibrium (zero-bias) value even with a relatively small bias of 50 mV. As Ting *et. al*. described in Ref. 22. the reduction of minority carrier density through exclusion and extraction to below the equilibrium level serves to reduce the diffusion dark current.

8. CONCLUSION

We demonstrated a LWIR i-CBIRD with the electrical junction in the wide-gap hole barrier region, away from the metallurgical hole-barrier/absorber heterojunction, which suppressed the generation-recombination dark current. Furthermore, the carrier exclusion and extraction effects are partially responsible for the observed low diffusion-limited CBIRD dark current despite short T2SL minority carrier lifetimes.

ACKNOWLEDGMENT

The authors thank R. Liang, R. Cox, T. Luchik, J. Fanson, M. Herman and E. Kolawa of JPL, and M. Tidrow of the U.S. Army Night Vision Electronics Sensor Directorate. The research was carried out at the Jet Propulsion

Laboratory, California Institute of Technology, under a contract with the National Aeronautics and Space Administration.

REFERENCES

[1] A. Rogalski, "Recent progress in infrared detector technologies", Proceedings of the International Conference on Quantum Structure Photodetectors(QSIP) 2010, Infrared Physics & Technology 54 (2011) 136-154.

[2] D.L. Smith and C. Mailhot, J. Appl. Phys., 62, pp. 2545, (1987)

[3] Meimie Z. Tidrow, Lucy Zheng, Hank Barcikowski, James Wells, Leslie Aitcheson, "Manufacture of Sb-Based Type II Strained Layer Superlattice Focal Plane Arrays"; CS ManTech Conference, May 18th-21st, 2009, Tampa, Florida

[4] P.-Y. Delaunay, B. M. Nguyen, D. Hoffman, E. K.-W. Huang, and M. Razegh, "Background Limited Performance of Long Wavelength Infrared Focal Plane Arrays Fabricated From M-Structure InAs–GaSb Superlattices"; IEEE J. Quantum Electron. 45, 157 (2009).

[5] Gunapala, S.D. Ting, D.Z. Hill, C.J. Nguyen, J. Soibel, A. Rafol, S.B. Keo, S.A. Mumolo, J.M. Lee, M.C. Liu, J.K. Yang, B. "Demonstration of a 1024 x 1024 Pixel InAs–GaSb Superlattice Focal Plane Array ",Photonics Technology Letters, IEEE, Vol. 22 Issue:24, (2010) 1865-1858.

[6] E. H. Aifer, I. Vurgaftman, C.L. Canedy, J.H. Warner, E.M. Jackson, J.G. Tischler, J.R. Meyer; "Recent progress in W-structured type-II superlattice photodiodes";Proc. SPIE Vol. 6479 (2007).

[7] E.H. Aifer, S.I. Maximenko, M.K. Yakes, C.Yi, C.L. Canedy, I Vurgaftman, E.M. Jackson, J.A. Nolde, C.A. Affouda, M. Gonzalez, J.R. Meyer, K.P Clark, P.R. Pinsukanjana,"Recent Developments in Type-II Superlattice Based Infrared Detectors", Proc. SPIE Vol. 7660, (2010)

[8] Alexander Soibel; David Z.-Y. Ting; Cory J. Hill; Mike Lee; Jean Nguyen; Sam A. Keo; Jason M. Mumolo; Sarath D. Gunapala;"High-performance long wavelength superlattice infrared detectors"; Proc.SPIE Vol. 7945, (2011),

[9] David Z. Ting, Cory J. Hill, Alexander Soibel, Sam A. Keo, Jason M. Mumolo, Jean Nguyen, Sarath D. Gunapala, Appl. Phys. Lett. 95, 023508 (2009).

[10] David Z. Ting, Cory J. Hill, Alexander Soibel, Jean Nguyen, Sam A. Keo, Michael C. Lee, Jason M. Mumolo, John, K. Liu, and Sarath D. Gunapala,"Antimonide-based barrier infrared detectors, Proc. SPIE Vol. 7660, (2010).

[11] B. Simolon, A. Aziz, R. Hansen, E. Kurth, S. Lam, S. Petronio, and J. Woolaway, "Standard format two-color CMOS ROIC for SLS detectors", Proceedings of the International Conference on Quantum Structure Photodetectors(QSIP) 2010, Infrared Physics & Technology 54 (2011) 306-309.

[12] Ronald G. Driggers, Paul Cox, and Timothy Edwards, Introduction to Infrared and Electro-Optical Systems (Artech House Optoelectronics Library), Artech House Publishers (1998).

[13] Michael J. Burke and William Wan, "IR FPA Sensor Characterization and Analysis using Matlab," SPIE Vol. 3377, p 71, (1998).

[14] Alexander Soibel, David Z.-Y. Ting, Cory J. Hill, Mike Lee, Jean Nguyen, Sam A. Keo, Jason M. Mumolo, and Sarath D. Gunapala, "Gain and noise of high-performance long wavelength superlattice infrared detectors" Appl. Phys. Lett. 96, 111102 (2010).

[15] John L. Vampola, "Readout Electronics for Infrared Sensor', The Infrared & Electro-Optical Systems Handbook, Vol.3 Electro-Optical Components, Ed. Willima D. Rogatto, SPIE Optical Engineering Press. (1993).

[16] Gerald C. Holst, "Infrared Imaging Testing",The Infrared & Electro-Optical Systems Handbook, Vol.4 Electro-Optical Systems Design, Analysis, and Testing, Ed. Michael C. Dudzik, SPIE Optical Engineering Press.(1993)

[17] Warren J. Smith, “Modern Optical Engineering The Design of Optical Systems” 2nd Edition”, McGraw-Hill (1990).

[18] S.B. Rafol; E. Cho, “Modulation transfer function measurement on QWIP focal plane array”, SPIE Proc. Vol. 6941, (2008).

[19] Mike Davis; Mark E. Greiner; John G. Sanders; James T. Wimmers, “ Resolution issues in InSb focal plane array system design”, Proc. SPIE Vol. 3379 (1998).

[20] H. Holloway,”Collection efficiency and crosstalk in closely spaced photodiode arrays”, J. App. Phys. 60, 1091 (1998).

[21] D. Donetsky, G. Belenky, S. Svensson, and S. Suchalkin, Appl. Phys. Lett. 97, 052108 (2010).